RSC Advances

PAPER

View Article Online
View Journal | View Issue

Cite this: *RSC Adv.*, 2025, **15**, 42493

Alginate-tungsten trioxide-reduced graphene-based membranes for PEM fuel cells operating above the boiling point of water

Wessam Nimir,[a] Tallah Magdi Ahmed,[b] Amani Al-Othman,[*ac] Muhammad Tawalbeh[de] and Sofian Kanan[f]

This study reports the fabrication and characterization of novel high-temperature proton exchange membranes composed of sodium alginate reinforced with tungsten trioxide-reduced graphene (WO_3-rG) nanocomposites, polyethylene glycol (PEG), and ionic liquids (ILs). The pristine sodium alginate (SA) membrane was first modified with varying concentrations of WO_3-rG to enhance its proton conductivity, mechanical characteristics, and thermal stability. The PEG was incorporated to improve flexibility and membrane hydration, along with diethylmethylammonium methanesulfonate ([DEMA][OMs]) IL. Additionally, characterization techniques were conducted, including proton conductivity (at ambient and elevated temperatures), swelling ratio, ion exchange capacity (IEC), water uptake, Fourier transform infrared (FTIR) spectroscopy, and tensile testing, to evaluate the membrane performance. The results show that the 3.23 wt% PEG/WO_3-rG/SA membrane exhibited the highest proton conductivity at room temperature, reaching 2.33×10^{-1} S cm^{-1} at 25 °C, while the IL/PEG/WO_3-rG/SA formulation demonstrated the most stable conductivity profile at elevated temperatures, maintaining 3.88×10^{-3} S cm^{-1} at 145 °C. In addition, the IL/PEG/WO_3-rG/SA membrane showed an excellent IEC of 1.65 meq g^{-1} and remarkable mechanical flexibility, with an elongation at break exceeding 768%. Therefore, these findings confirm the positive role of WO_3-rG, IL, and PEG in the membrane's structure and enhancing its functional properties, as well as improving its flexibility. The work showed that the IL/PEG/WO_3-rG/SA composite is a promising candidate for high-temperature proton exchange membrane (HT-PEM) fuel cell applications, especially those operating above the boiling point of water.

Received 25th July 2025
Accepted 22nd October 2025

DOI: 10.1039/d5ra05401j

rsc.li/rsc-advances

1. Introduction

Fuel cells are widely recognized as promising energy systems for clean and efficient power generation.[1,2] Among them, proton exchange membrane fuel cells (PEMFCs) are particularly appealing to researchers because they offer high power output, quick startup capabilities, and a low carbon footprint or environmental effects.[3,4] In recent years, high-temperature proton exchange membrane fuel cells (HT-PEMFCs), which operate above 100 °C (*i.e.*, above the boiling point of water), have attracted attention as a viable alternative to low-temperature PEMFCs.[5–7] This high temperature operation allows enhanced kinetics,[8] reduces the sensitivity to carbon monoxide poisoning, and simplifies the thermal and water management because water will be formed in the vapor phase rather than accumulating as a liquid in the cathode.[9] This makes HT-PEMFCs particularly suitable for transportation and stationary power applications.[10] Despite these advantages, their practical application in multiple sectors remains delayed by the lack of proper electrolyte membranes that maintain both a reasonable proton conductivity and the mechanical integrity under elevated and anhydrous conditions. Although Nafion is considered the current benchmark PEM for low-temperature fuel cells, it still suffers from degradation, and a sharp decrease in conductivity at high temperatures is observed due to the evaporation of its water content.[11,12] This limitation has led to a growing interest in the development of alternative materials to Nafion that are capable of operating efficiently above the boiling point of water, and also in dry environments.[13,14]

Biopolymer-based membranes, particularly those derived from natural sources, have emerged as attractive candidates because they are environmentally friendly, have tunable

[a]*Department of Chemical and Biological Engineering, American University of Sharjah, PO Box 26666, Sharjah, United Arab Emirates. E-mail: aalothman@aus.edu*

[b]*Engineering Systems Management Graduate Program, American University of Sharjah, PO Box 26666, Sharjah, United Arab Emirates*

[c]*Energy, Water and Sustainable Environment Research Center, American University of Sharjah, PO Box 26666, Sharjah, United Arab Emirates*

[d]*Sustainable and Renewable Energy Engineering Department, University of Sharjah, PO Box 27272, Sharjah, United Arab Emirates*

[e]*Sustainable Energy & Power Systems Research Centre, RISE, University of Sharjah, PO Box 27272, Sharjah, United Arab Emirates*

[f]*Department of Biology, Chemistry and Environmental Sciences, American University of Sharjah, PO Box 26666, Sharjah, United Arab Emirates*

properties, and are available at a low cost.[15] One of these materials is sodium alginate (Na-Alg), a naturally derived polysaccharide obtained from brown algae, which has demonstrated potential in membrane development.[16] It offers intrinsic proton-conducting behavior and high water-retention properties.[17,18] However, its insufficient thermal and mechanical stability under high temperature operating conditions dictates the need for structural reinforcement by incorporating fillers.[19] Smitha *et al.*[20] developed various membranes using a blend of sodium alginate and deacetylated chitosan. The formulation with 84% deacetylated chitosan exhibited notable performance, with a water uptake (WU) of 32%, an ion exchange capacity of 1.40 meq g^{-1}, and a proton conductivity of 4.20×10^{-2} S cm^{-1}. Similarly, Zhu *et al.*[18] employed a crosslinking approach to incorporate MXene nanosheets into a cellulose nanofiber/sodium alginate matrix, enabling the construction of heterogeneous membranes with ordered polymer channels and tightly stacked 2D layers. The resulting composite membrane demonstrated excellent mechanical strength of 164.7 MPa and achieved a proton conductivity of 4.54×10^{-2} S cm^{-1}. Hence, this study presents the development of novel SA-based composite membranes incorporating tungsten trioxide-reduced graphene (WO_3-rG), ionic liquids (ILs), and polyethylene glycol (PEG) to overcome the existing limitations.

Tungsten trioxide (WO_3), on the other hand, is a transition metal oxide, which is well-known for its high proton affinity, electrochemical stability, and catalytic behavior.[21] Previous studies in the literature demonstrated that the integration of WO_3 nanoparticles into the polymer matrix has improved proton conductivity as well as the thermal stability due to the formation of additional proton conduction paths and strong interfacial interactions.[21,22] For instance, several studies explored the enhancement of Nafion-based membranes through the incorporation of WO_3 as an inorganic additive. Shao *et al.*[23] prepared Nafion composite membranes by blending WO_3, along with other oxides such as silicon dioxide (SiO_2) and titanium dioxide (TiO_2), through a recasting method. Characterization using scanning electron microscope (SEM) and X-ray diffraction (XRD) confirmed uniform oxide distribution and increased membrane crystallinity. Moreover, thermogravimetric analysis (TGA) showed a thermal degradation in membranes containing WO_3 and TiO_2 at an earlier temperature compared to the Nafion membrane. These modified membranes exhibited enhanced WU relative to unmodified Nafion. In another study by Selim *et al.*,[24] hybrid membranes consisting of Nafion and nanosized WO_3 particles showed a 21% increase in WU, reduced swelling ratio (SR), and significantly enhanced mechanical stability relative to commercial Nafion. However, the integration of WO_3 into biopolymer-based membranes remains relatively unexplored. On the contrary, the combination of WO_3 with reduced graphene (rG), forming WO_3-rG, has attracted attention in recent years due to the synergistic effects between these two materials.

Reduced graphene (rG) and reduced graphene oxide (rGO) are known materials in the development of advanced PEMs for fuel cell applications. Their unique structural properties, such as high surface area, excellent electrical conductivity, and the presence of oxygenated functional groups, make them ideal candidates for enhancing the performance of PEMs.[25] The synthesis of rG typically involves the chemical or thermal reduction of graphene oxide (GO). Chemical reduction methods often utilize agents like hydrazine or ascorbic acid to restore the sp^2 hybridization of carbon atoms, thereby enhancing electrical conductivity. For example, Samancı *et al.*[26] explored the synthesis of rG through chemical reduction processes, highlighting the significant improvements in conductivity and structural integrity achieved through these methods. Thermal reduction, on the other hand, involves heating GO at elevated temperatures to remove oxygen-containing groups, leading to the restoration of the graphene lattice. This method has been extensively studied for its efficiency in producing high-quality rG with minimal defects.[27] The structural characteristics of rG, including the degree of reduction and the presence of residual oxygen functionalities, play a crucial role in determining its suitability for specific applications in PEMs. While rG offers enhanced electronic properties, rGO retains a higher density of oxygenated groups, which are instrumental in proton conduction. The presence of these functional groups facilitates the formation of hydrogen bonds with water molecules, promoting proton transport through the membrane.[28] For instance, Ri *et al.*[29] conducted first-principles calculations to investigate proton migration on water-adsorbed monolayer and bilayer rGO sheets, revealing that water molecules adsorbed on rGO sheets facilitate proton hopping *via* low-activation-energy pathways, suggesting that rGO can complement rG by providing proton conduction channels alongside the electronic network.

The integration of rG and rGO into PEMs not only enhances proton conductivity but also improves the catalytic properties of the membrane. The bifunctional effect of rGO, where both graphitization and oxygenated groups contribute to the catalytic activity and stabilization of metal nanoparticles, has been demonstrated by He *et al.* This dual functionality is particularly beneficial in fuel cell applications, where efficient catalysis is essential for optimal performance.[25] Furthermore, the incorporation of rG into polymer matrices has been shown to improve the mechanical strength and thermal stability of PEMs. Recent studies have focused on the development of composite membranes incorporating rG and rGO to leverage their synergistic effects. For example, Prasad *et al.*[30] investigated the electrochromic performances of rGO-WO_3 thin films, demonstrating their potential as integrated devices powered by quantum dot-sensitized solar cells. This research underscores the versatility of rGO-based composites in various energy-related applications. Looking forward, the continued exploration of rG and rGO in PEMs holds promise for the advancement of fuel cell technologies. Future research should aim to optimize the synthesis methods to achieve desired structural characteristics, enhance the understanding of proton conduction mechanisms, and develop composite membranes that offer improved performance and durability.

This work focuses on the synthesis and characterization of WO_3-rG/SA-based composite membranes containing ILs and PEG to further investigate membrane conductivity under anhydrous conditions. ILs are characterized by their very low-

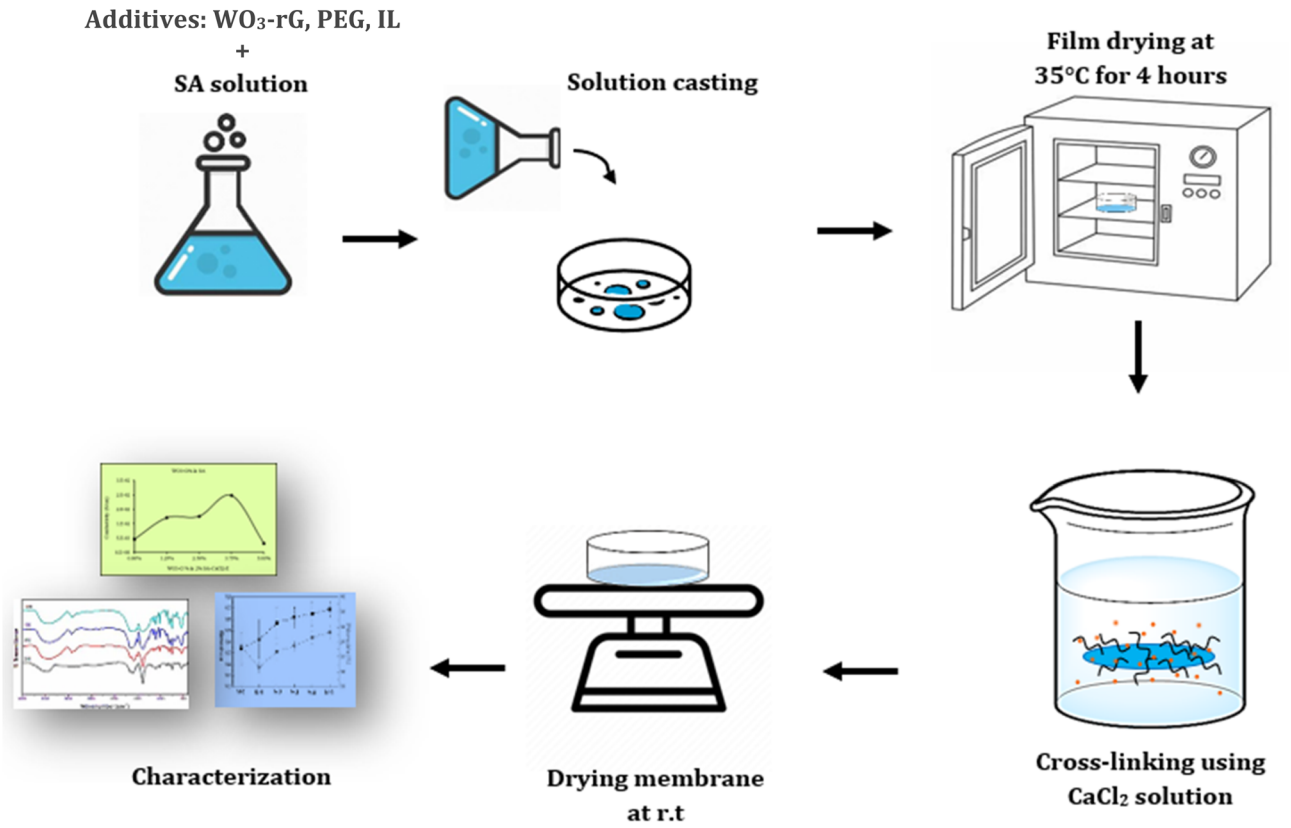

Fig. 1 Schematic diagram of the membrane fabrication procedure.

volatile nature, high thermal stability, and excellent ionic conductivity.[31] They are effective dopants that can form extensive hydrogen-bond networks, which promote proton mobility within structures.[32] ILs are known structure directing agents too. Additionally, PEG is a plasticizing agent that improves membrane flexibility and mechanical strength.[33] It contributes to maintaining internal hydration and creates additional proton conduction pathways.[34] Therefore, the present work systematically evaluates the membranes in terms of proton conductivity at ambient and elevated temperatures, WU, SR, ion exchange capacity, Fourier transform infrared spectroscopy (FTIR) analysis, and mechanical strength. This work aims to characterize and determine the suitability of the proposed composite for the application in high-temperature proton exchange membrane fuel cells.

2. Methodology and experimental

2.1 Materials

Sodium alginate, serving as the main polymer matrix, was sourced from Sigma Aldrich. The ionic liquid diethyl methyl ammonium methanesulfonate ([DEMA][OMs]) was acquired from IoLiTec-ILs Technologies GmbH, while polyethylene glycol (PEG, CAS No. 25322-68-3), graphite, sodium tungstate, DOWEX-200, and ascorbic acid were purchased from Sigma Aldrich. Additional reagents, including solvents and cross-linking agents, were acquired from commercial sources and used as received without further purification.

2.2 Synthesis of tungsten trioxide-reduced graphene

Graphene was produced *via* oxidation of graphite following the well known Hummers' method.[35] In brief, 1.0 g graphite powder was placed in a round-bottom flask with 30 mL concentrated sulfuric acid along with 0.5 g sodium nitrate, and the mixture was stirred at room temperature for 30 min. 1.0 g potassium permanganate in 50 mL aqueous solution was added slowly under stirring and cooling for 3 hours. The produced graphene was isolated using a 5000 rpm centrifuge. The solid was dried at 50 °C for 24 hours, then reduced using ascorbic acid solution and annealed at 350 °C. Around 2 moles of tungstic acid were prepared by cation exchange of sodium tungstate using DOWEX-200 resin at pH 3.5. The prepared tungstic acid was mixed with an aqueous oxalic acid solution, mixed with 0.5 g of the above reduced graphene (rG) under vigorous stirring. The solution was stirred at 2000 rpm for 72 hours, followed by an annealing at 500 °C, ramping the temperature by 5 °C min^{-1}.

2.3 Fabrication of membranes

The membranes were fabricated using the simple casting and external gelation technique as reported by Li *et al.*[36] First, 2 g of sodium alginate was dissolved in 100 mL of distilled water, stirred at 25 °C for 6 hours to form a 2% solution, and then filtered through a 0.45 μm membrane filter and degassed under vacuum to remove air bubbles. Next, the solution was evenly cast onto Petri dishes, ensuring consistent volume for uniform film thickness, and dried in the oven at 35 °C for 24 hours. After

drying, the films were crosslinked by immersing them in a 1.5% calcium chloride solution (prepared by dissolving 1.5 g of $CaCl_2$ in 100 mL of a 30% ethanol–water mixture) for 1 hour at room temperature, followed by rinsing with deionized water three times to remove residual calcium ions and drying at ambient conditions. The procedure is illustrated in Fig. 1. To incorporate WO_3-rG, varying amounts were mixed directly into the sodium alginate solution before casting, ensuring thorough stirring for uniform dispersion. The films underwent the same casting and crosslinking procedures to form WO_3-rG/SA composite membranes, which were then ready for further characterization and testing.

2.4 Characterization of membrane functionality and morphology

A series of comprehensive characterization techniques was employed to evaluate the performance and properties of the synthesized WO_3-based composite membranes, focusing on their structural, chemical, and functional attributes. These techniques are as follows:

2.4.1 Water absorption and swelling behavior. The WU and SR of the membranes were evaluated to assess their hydration behavior and dimensional stability. Initially, the membranes were immersed in distilled water at room temperature for 24 hours. After immersion, the membranes were gently blotted to remove excess surface water, and the wet weight of each membrane was recorded. The membranes were then dried at 100 °C for 1 hour, and their dry weight was recorded afterward. The WU was determined by comparing the dry weight to the wet weight. This procedure is similar to the method reported by ref. 37–39, where water absorption was used to assess membrane performance. The water uptake percentage (WU) was calculated as the percentage increase in weight, using eqn (1):

$$\mathrm{WU} = \frac{W_{\mathrm{wet}} - W_{\mathrm{dry}}}{W_{\mathrm{dry}}} \times 100 \quad (1)$$

where w_{wet} is the weight of the membrane after immersion, and w_{dry} is the initial dry weight. All masses are reported in grams. For example (SA sample, Table 2): $w_{\mathrm{wet}} = 0.0112$ g and $w_{\mathrm{dry}} = 0.0072$ g, hence, WU = (0.0112–0.0072)/0.0072 × 100% = 55.6%. On the other hand, to evaluate the SR, the dimensional changes of the membranes in the hydrated state were measured. The SR was calculated using eqn (2):

$$\mathrm{SR} = \frac{S_{\mathrm{wet}} - S_{\mathrm{dry}}}{S_{\mathrm{dry}}} \times 100 \quad (2)$$

where S_{dry} and S_{wet} represent the length of the membrane before and after water absorption, respectively. The swelling behavior and water absorption properties were analyzed at different intervals of immersion to investigate the stability and long-term hydration behavior of the membranes.

2.4.2 Ion exchange capacity. The ion exchange capacity (IEC) provides a quantitative measure of the membrane's ability to exchange protons, which is critical for evaluating its proton conduction potential. In this study, IEC was determined using a titration-based method. Small membrane specimens were first dried in an oven at 100 °C for five hours, and their dry mass was recorded. Each sample was then soaked in a 2.0 M sodium chloride (NaCl) solution for 48 hours at ambient conditions to replace the protons in the membrane with sodium ions (Na^+). The resulting solution was titrated with a 0.01 M sodium hydroxide (NaOH) solution using anthocyanin, which is a natural pH indicator derived from red cabbage. The IEC value was determined using eqn (3):

$$\mathrm{IEC} = \frac{V_{\mathrm{NaOH}} - N_{\mathrm{NaOH}}}{m_{\mathrm{dry}}} \times 100 \quad (3)$$

where V_{NaOH} is the volume of NaOH used in liters, N_{NaOH} is the normality of the NaOH solution (meq L^{-1}), and m_{dry} is the dried weight of the membrane sample in grams. The titration volumes corresponding to the membrane samples are reported in Table 1.

2.4.3 Proton conduction through electrochemical impedance spectroscopy. The proton conductivity of the synthesized membranes was tested using electrochemical impedance spectroscopy (EIS). For the test, the membrane was cut to size and placed between two stainless-steel electrodes within a custom-made cell. Impedance measurements were conducted using a BioLogic SP-200 Potentiostat linked to EC-Lab Software (version 11.10), covering a frequency range from 0.0001 to 7 MHz. Next, the impedance data obtained from the measurement were plotted on a Nyquist plot, where the intersection with the *x*-axis in the high-frequency region provided the membrane's bulk resistance, *R*. Since the cell configuration used for measuring proton conductivity and the thickness of each membrane were kept constant for all measurements. This allows the proton conductivity σ to be calculated using eqn (4):

$$\sigma = \frac{t}{R \times A} \quad (4)$$

Here, *R* is the bulk resistance (Ω) obtained from the high-frequency intercept of the Nyquist plot, *A* is the electrode contact area (1.13 cm^2), and *t* is the average membrane

Table 1 Titration volumes and dry masses for the membrane samples

Membrane	m_{dry} (g)	IEC (meq g^{-1})	NaOH conc. (M)	V_{NaOH} (L)	V_{NaOH} (mL)
SA	0.0072	1.37	0.01	0.000986	0.986
WO_3-rG/SA	0.0069	1.56	0.01	0.001076	1.076
PEG/WO_3-rG/SA	0.0055	1.13	0.01	0.0006215	0.6215
IL/WO_3-rG/SA	0.0084	1.42	0.01	0.0011928	1.193
IL/PEG/WO_3-rG/SA	0.0097	1.66	0.01	0.0016102	1.610

thickness (0.02 cm = 200 μm). Impedance measurements were performed in the frequency range 0.0001 Hz–7 MHz, and the temperature dependent measurements were carried out between 80 °C and 150 °C in 10 °C steps, using a BioLogic ITS climate chamber. This method was consistent with the procedure employed for EIS testing. For clarity, a worked example is given for the pristine SA membrane at 25 °C: $R = 3.91\ \Omega$ (from the Nyquist plot), therefore $\sigma = t/(R \times A) = 0.02/(3.91 \times 1.13) = 4.53 \times 10^{-3}$ S cm^{-1}.

2.4.4 Fourier transform infrared spectroscopy. The FTIR was employed to investigate the chemical structure and confirm the presence of functional groups in the synthesized membranes. The spectra were recorded using a PerkinElmer Spectrum One FTIR Spectrometer across the spectral range of 4000–450 cm^{-1}.

2.4.5 Mechanical properties and strength. Evaluating the mechanical integrity of the membranes is essential to understanding their resistance to deformation and overall durability. In this work, tensile testing was performed using an Instron 5582 Universal Testing Machine under quasi-static loading conditions. Rectangular membrane strips were steadily pulled apart until failure, and the force–displacement data were converted to stress–strain curves. From these plots, the tensile strength, Young's modulus, and elongation at break were extracted to characterize the membranes' flexibility and structural reliability.

3. Results and discussion

3.1 Water uptake and swelling ratio results

A large set of membranes with varying compositions was synthesized and initially screened based on their proton conductivity performance. The best-performing membranes from each composition were then selected for further physicochemical characterization, including WU, SR, and IEC. For clarity and consistency with literature convention, these parameters are presented first in the Results section, followed by a detailed discussion of the conductivity results, which can be found in the preceding sections. The WU and SR results are recorded in Table 2. In terms of WU, the SA membrane exhibited the highest WU of 56%, highlighting its strong hydrophilic nature. However, the incorporation of 3.75 wt% WO_3-rG led to a significant decrease in WU to 25%, indicating that the addition of tungsten oxide/reduced graphene introduced hydrophobicity, reducing the membrane's water retention capability. Further modifications with IL and PEG resulted in distinct trends. The IL/WO_3-rG/SA membrane displayed the lowest WU at 18%, which aligns with the observed drop in proton conductivity. This decrease suggests that the IL content restricted water absorption, potentially due to hydrophobic interactions that limited free water availability for proton transport. Conversely, the addition of PEG increased WU. The PEG/WO_3-rG/SA membrane exhibited a WU of 46%, which is notably higher than the 3.75 wt% WO_3-rG/SA membrane (25%). This increase can be attributed to PEG's plasticizing effect, which enhances the membrane's water retention capability. Finally, the IL/PEG/WO_3-rG/SA membrane demonstrated a further increase in WU to 43%, showing that PEG's hydrophilic nature counterbalanced the hydrophobic effects of IL.

On the other hand, the SR reflects the extent of dimensional expansion upon hydration, which affects mechanical integrity and fuel cell performance. The SA membrane exhibited the lowest SR at 23%, suggesting good structural stability. However, the incorporation of 3.75 wt% WO_3-rG resulted in an increase in the SR to 44%, which is likely due to the interaction between the polymer matrix and the added inorganic filler, affecting the cross-linking density. A more pronounced increase in SR was observed with the addition of PEG. The PEG/WO_3-rG/SA membrane exhibited an SR of 69%, which is the second highest SR among all membranes. This indicates that PEG's plasticizing effect enhanced the membrane's flexibility but also increased dimensional expansion, which may compromise mechanical stability at high WU levels. In addition, the IL/WO_3-rG/SA membrane showed an SR of 43%, demonstrating a balance between WU reduction and maintaining reasonable dimensional stability. The highest SR of 78% was recorded for the IL/PEG/WO_3-rG/SA membrane, attributed to the combined effect of PEG's water retention properties and IL's potential cross-linking interactions within the polymer matrix.

3.2 Ion exchange capacity

The IEC is a critical parameter reflecting the number of available ion-exchange sites in a membrane, which directly affects proton conductivity. The IEC values of the synthesized membranes varied depending on the composition and presence of additives, ranging from 1.13 to 1.65 meq g^{-1}. As shown in Table 3, the pristine SA membrane exhibited an IEC of 1.37 meq g^{-1}, attributed to the presence of carboxylic groups along the alginate backbone. Incorporation of WO_3-rG into the SA matrix slightly increased the IEC to 1.56 meq g^{-1}, indicating enhanced ion-exchange functionality, possibly due to better dispersion and interfacial interaction with the polymer. Interestingly, the

Table 2 Comparison of water uptake analysis and swelling ratio for the synthesized membranes

Composition	Hydrated sample (g)	Dried sample (g)	WU (%)	Hydrated sample (g)	Dried sample (g)	SR (%)
SA	0.0112	0.0072	56	2.25	1.82	23
WO_3-rG/SA	0.0086	0.0069	25	2.72	1.89	44
PEG/WO_3-rG/SA	0.0065	0.0055	18	2.64	1.56	69
IL/WO_3-rG/SA	0.0123	0.0084	46	2.32	1.62	43
IL/PEG/WO_3-rG/SA	0.0139	0.0097	43	2.56	1.44	78

Table 3 The ion exchange capacity of pristine SA and synthesized membranes

Membrane	WU (%)	IEC (meq g^{-1})	Ref.
Nafion 117	29	0.91	41
SPEEK	36.02	2.15	42
SA	56	1.37	This work
WO_3-rG/SA	25	1.56	This work
PEG/WO_3-rG/SA	18	1.13	This work
IL/WO_3-rG/SA	46	1.42	This work
IL/PEG/WO_3-rG/SA	43	1.66	This work

addition of PEG led to a reduction in IEC to 1.13 meq g^{-1}, likely due to PEG's non-ionic nature, which can dilute the density of active sites within the membrane matrix. In addition, the inclusion of IL significantly influenced IEC values. The IL/WO_3-rG/SA membrane recorded 1.42 meq g^{-1}, while the IL/PEG/WO_3-rG/SA membrane achieved the highest IEC value of 1.65 meq g^{-1}, demonstrating a synergistic effect between IL and the filler network. The presence of IL likely introduced additional proton-conducting pathways and enhanced membrane hydrophilicity, leading to more accessible exchangeable sites. While the WU results of the prepared membranes are comparable to those of Nafion 117, which typically exhibits WU in the range of 22–29%, the IEC values reported here are notably higher than Nafion's reported value of 0.91 meq g^{-1}. One possible explanation is that the number of active functional groups present in the polymer matrix, particularly in the IL-containing membranes, exceeds those typically found in Nafion.[40]

3.3 Proton conductivity results at 25 °C

Proton conductivity at 25 °C provides a baseline for evaluating membrane performance under ambient conditions. Therefore, the membranes were measured at room temperature (25 ± 2 °C) under ambient relative humidity (40–60% RH). Before testing, they were kept in sealed zipper bags to maintain consistent hydration levels across all samples. This section presents the conductivity values of SA-based membranes modified with WO_3-rG, IL, and PEG, highlighting the impact of each additive on proton transport efficiency.

3.3.1 Effect of WO_3-G on SA membranes. Proton conductivity is an important parameter for evaluating the performance of membrane materials in PEMFCs. Accordingly, the conductivities of 2 wt% SA membranes with varying amounts of WO_3-rG were measured to assess the effect of this composite filler on proton transport. The Nyquist plot and the equivalent circuit diagram for Pristine SA are shown in Fig. 2(a) and (b), respectively. The conductivity generally increased with WO_3-rG loading up to a certain point, highlighting the positive role of the filler. The pure SA membrane exhibited the lowest conductivity at 4.52×10^{-3} S cm^{-1}, with a resistance of 3.91 Ω, reflecting limited intrinsic proton transport.[43] The resistances were obtained from the Nyquist plot as mentioned earlier in this context. In addition, introducing 1.25 wt% WO_3-rG reduced the resistance to 1.21 Ω and increased conductivity by nearly threefold to 1.21×10^{-2} S cm^{-1}. Further increasing the filler to 2.5 wt% slightly improved conductivity to 1.26×10^{-2} S cm^{-1}. The highest conductivity recorded was at 3.75 wt% WO_3-rG,

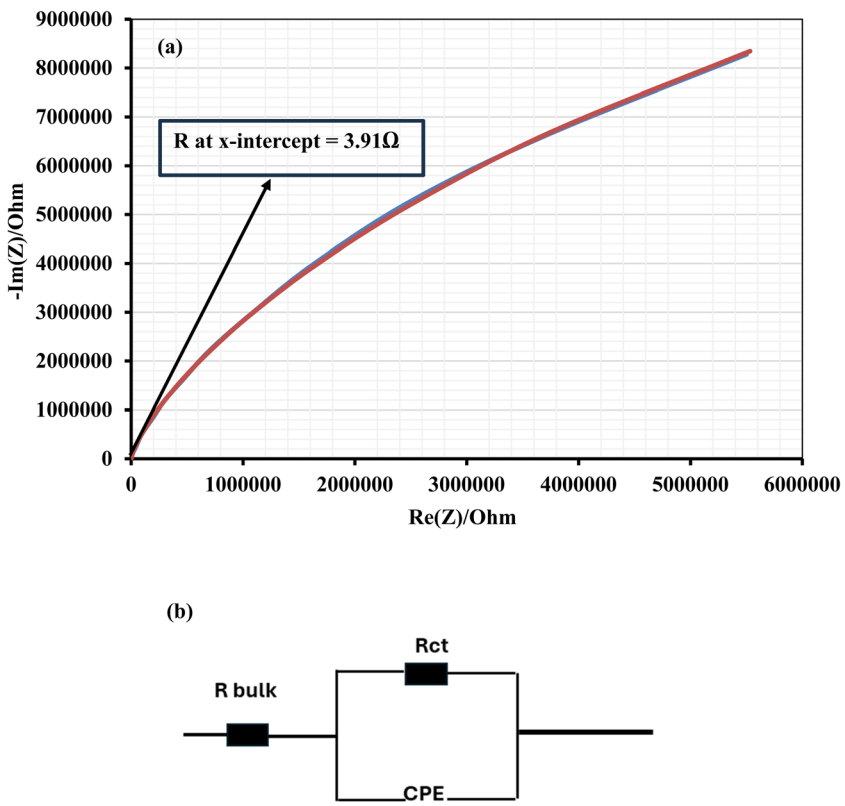

Fig. 2 (a) Nyquist plot and (b) a simple equivalent circuit diagram for pristine SA. R = 3.91 Ohm. Conductivity = 4.52×10^{-3} S cm^{-1}.

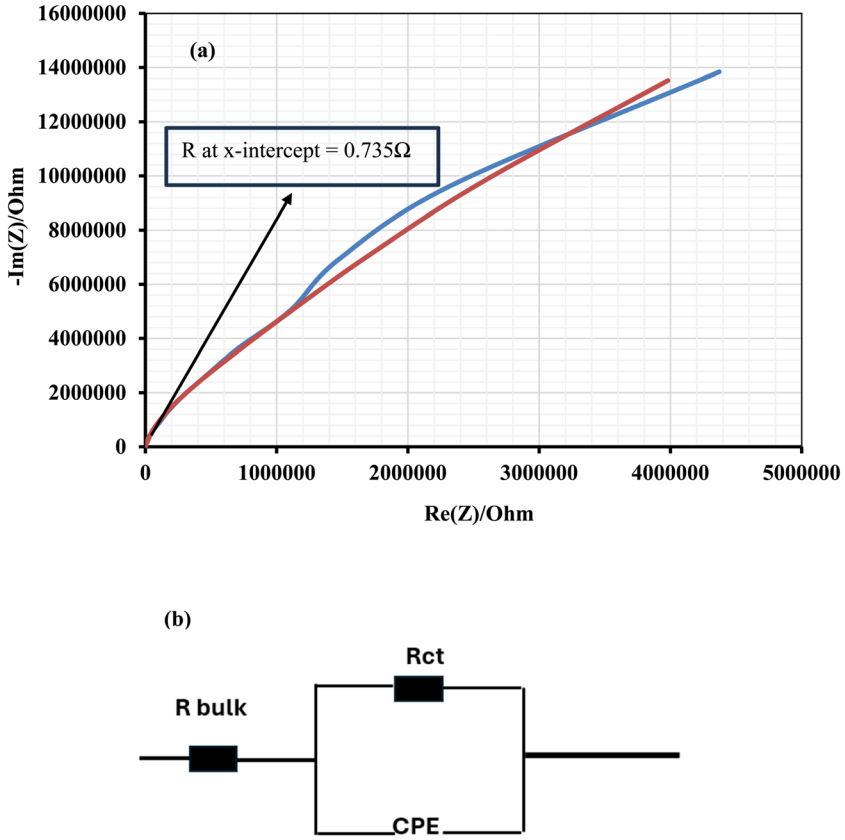

Fig. 3 (a) The Nyquist plot and (b) a simple equivalent circuit diagram for the 3.75 wt% WO_3-rG/SA membrane. R bulk (at the high frequency region) = 0.735 Ohm. Conductivity = 1.98×10^{-2} S cm^{-1}.

reaching 1.98×10^{-2} S cm^{-1}, with a significantly reduced resistance of 0.735 Ω. Fig. 3(a) and (b) show the Nyquist plot and the equivalent circuit diagram for the 3.75 wt% WO_3-G/SA membrane, respectively. Hence, this indicates optimal filler dispersion and formation of continuous proton-conducting pathways. The enhancement can be attributed to acid–base interactions from WO_3 that facilitate proton hopping, and the high surface area of graphene that supports water retention and network continuity.[44] However, at 5 wt% WO_3-rG, conductivity dropped sharply to 3.10×10^{-3} S cm^{-1}, while resistance increased to 4.71 Ω. This suggests that excess filler led to agglomeration, disrupting conductive pathways, and possibly increasing tortuosity within the membrane matrix.[45] While 3.75 wt% WO_3-rG shows the highest conductivity among the tested concentrations, further optimization of the WO_3-rG concentration could yield even higher conductivity values. Small variations in the WO_3-rG loading may improve proton transport by further enhancing the filler dispersion or altering the membrane's structural properties.

3.3.2 Effect of PEG on WO_3-rG/SA membranes. To further enhance the proton conductivity and possibly the dispersion of the WO_3-rG, PEG was introduced as a plasticizer into the optimized membrane composition from the previous section, which contained 3.75 wt% WO_3-rG/SA. This formulation had already demonstrated promising conductivity (1.98×10^{-2} S cm^{-1}) and relatively low resistance (0.735 Ω). The PEG is expected to also improve proton mobility by increasing membrane flexibility and WU due to its hydrophilic nature.[46] It is also reported that PEG increases the membrane's wettability.[47] The results showed that the addition of 1.78 wt% PEG, a slight decrease in conductivity was observed (1.39×10^{-2} S cm^{-1}), accompanied by an increase in resistance to 1.65 Ω. This initial decline could be due to partial disruption of the conductive pathways without sufficient PEG to form a continuous hydrated network. However, at 3.23 wt% PEG, the membrane showed a significant performance improvement as the proton conductivity rose to 1.03×10^{-1} S cm^{-1}, with a low resistance of 0.172 Ω, which is almost five times the initial value. This indicates that optimal PEG content effectively enhances proton transport by facilitating segmental motion and water retention. The Nyquist plot for 3.23 wt% PEG/WO_3-rG/SA membrane is presented in Fig. 4. At a higher PEG concentration of 4.70 wt%, the conductivity declined to 3.50×10^{-3} S cm^{-1}. This performance drop suggests that excess PEG may lead to phase separation, excessive swelling, or blockage of proton-conducting channels, ultimately hindering transport efficiency. These findings demonstrate that a balanced amount of PEG is crucial, with 3.23 wt% identified as the most favorable for achieving high conductivity and low resistance.

3.3.3 Effect of ILs on WO_3-rG/SA and PEG/WO_3-rG/SA membranes. To evaluate the impact of ILs on membrane performance, diethyl methyl ammonium methanesulfonate

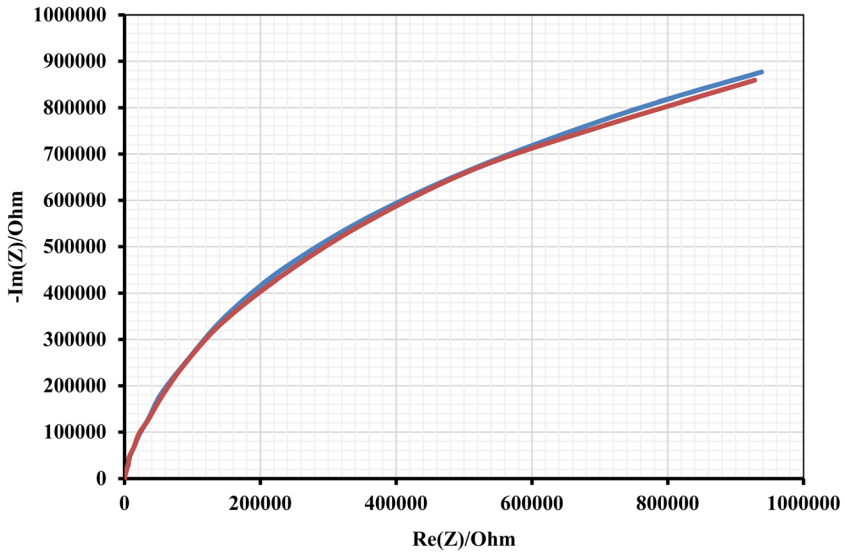

Fig. 4 The Nyquist plot for the 3.23 wt% PEG/WO_3-rG/SA membrane. R = 0.172 ohm, conductivity = 1.03 × 10^{-1} S cm^{-1}.

([DEMA][OMs]) was incorporated in increasing amounts into both the WO_3-rG/SA membrane and the PEG/WO_3-rG/SA composite, using the best-performing membranes from previous experiments as the base formulations. In the absence of IL, the WO_3-rG/SA membrane with 3.75 wt% filler showed a conductivity of 1.98 × 10^{-2} S cm^{-1} and a resistance of 0.735 Ω. However, the addition of IL resulted in a steady decline in conductivity with increasing IL content, as seen in Fig. 5. At 1.29 wt% IL, the conductivity dropped to 1.01 × 10^{-2} S cm^{-1}, and the resistance increased to 2.27 Ω. Further increases to 2.82 wt% and 4.33 wt% IL resulted in sharp increases in resistance, and correspondingly lower conductivities of 3.97 × 10^{-3} and 2.30 × 10^{-3} S cm^{-1}. This reduction suggests that excess IL may disrupt the membrane's microstructure, possibly due to IL aggregation or phase separation, which can hinder the formation of efficient proton-conducting pathways.

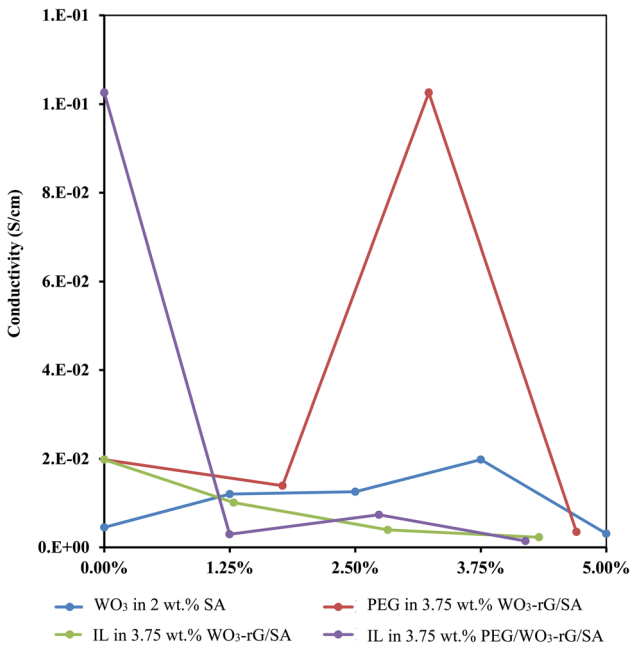

Fig. 5 The effect of WO_3-rG, PEG, and IL content on the conductivity (S cm^{-1}) of the fabricated membranes.

On the other hand, the PEG-modified membrane without IL showed the highest conductivity among all tested membranes at 1.03 × 10^{-1} S cm^{-1}, with a low resistance of 0.172 Ω. However, Fig. 5 also shows that upon IL addition, a similar downward trend in performance was observed. At 1.25 wt% IL, the conductivity fell drastically to 2.96 × 10^{-3} S cm^{-1}. Additionally, increasing the IL content to 2.74 wt% yielded a modest improvement in conductivity of 7.37 × 10^{-3} S cm^{-1}. A further increase to 4.20 wt% IL led to a severe conductivity drop to 1.45 × 10^{-3} S cm^{-1}, along with a high resistance of 20.72 Ω. These results indicate that while ILs can enhance conductivity in some polymer systems, their addition to WO_3-rG/SA and PEG/WO_3-rG/SA membranes under these conditions was slightly negative. The trend suggests that ILs in these composites may interfere with the established proton-conducting network, as they are known to be structure directing agents, particularly when not properly integrated or when used in excess, leading to structural instability and reduced transport efficiency. This effect is evident in SEM images (Fig. S-1–S-5 in the SI), where the introduction of ILs alters the morphology of the membranes.

The distinct roles of PEG, IL, and WO_3-rG can be explained based on previous studies. For instance, PEG, with its hydrophilic nature, can enhance the flexibility and water retention properties at lower temperatures but also promotes swelling at elevated temperatures.[34] Additionally, ILs are thermally stable and contribute towards proton hopping even under low hydration conditions.[48] The WO_3-rG nanoparticles provide the structural reinforcements and hydrophilic fillers, generating multiple hydrogen-bonding networks that would facilitate proton transport within the membrane matrix.[49] Overall, and to summarize, WU and SR are important properties for the membrane. The WU affects the conductivity because water

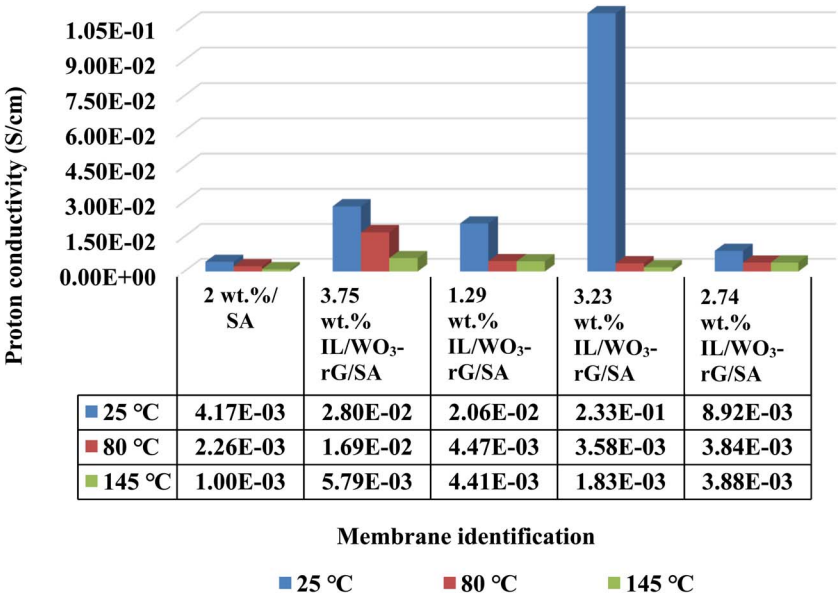

	2 wt.%/ SA	3.75 wt.% IL/WO_3-rG/SA	1.29 wt.% IL/WO_3-rG/SA	3.23 wt.% IL/WO_3-rG/SA	2.74 wt.% IL/WO_3-rG/SA
25 °C	4.17E-03	2.80E-02	2.06E-02	2.33E-01	8.92E-03
80 °C	2.26E-03	1.69E-02	4.47E-03	3.58E-03	3.84E-03
145 °C	1.00E-03	5.79E-03	4.41E-03	1.83E-03	3.88E-03

Fig. 6 Summary of proton conductivity for the best-performing membranes at 25, 80, and 145 °C.

provides paths for proton hopping. Swelling can enhance the proton conduction; however, it is not the most significant factor. It should also be noted in this context that WU and SR do not complement each other. In fact, excessive SR affects the membrane's mechanical integrity.

3.4 Proton conductivity results at elevated temperatures

As temperature increases, the proton conduction mechanism can be influenced by various factors such as membrane hydration, segmental motion of polymer chains, and the stability of conductive pathways. Temperature-dependent measurements (25–150 °C) were performed under ambient and conventional relative humidity conditions in the laboratory (40–60%). Membranes were stored in sealed zipper bags prior to measurement and tested immediately to maintain consistent hydration conditions. The best-performing membrane from each composition, determined based on its conductivity at 25 °C, was subjected to high-temperature conductivity measurements to evaluate its thermal stability and performance. The results are demonstrated in Fig. 6. The pristine SA membrane exhibited a sharp decline in proton conductivity with increasing temperature. At 25 °C, the conductivity was 4.17×10^{-3} S cm^{-1}; however, as the temperature reached 80 °C, it dropped to 2.26×10^{-3} S cm^{-1}, and at 145 °C, it further decreased to 1.00×10^{-3} S cm^{-1}. This reduction suggests that SA alone struggles to maintain adequate proton conductivity at elevated temperatures, likely due to dehydration effects and the absence of additional proton-conducting pathways. Moreover, 3.75 wt% WO_3-rG/SA membrane demonstrated superior conductivity compared to pristine SA, starting at 2.80×10^{-2} S cm^{-1} at 25 °C. However, as the temperature increased, the conductivity gradually declined to 1.69×10^{-2} S cm^{-1} at 80 °C and 5.79×10^{-3} S cm^{-1} at 145 °C. This decline is attributed to reduced water retention and limited polymer chain mobility at higher temperatures. Despite the decrease, this membrane outperformed pure SA, likely due to the presence of WO_3-rG, which contributed to an extended proton transport network. On the other hand, the 1.29 wt% IL/WO_3-rG/SA membrane, which started with a proton conductivity of 2.06×10^{-2} S cm^{-1} at 25 °C. At 80 °C, it decreased significantly to 4.47×10^{-3} S cm^{-1} and further declined to 4.41×10^{-3} S cm^{-1} at 145 °C. While IL initially facilitates proton transfer, partial phase separation or limited retention at higher temperatures reduces overall conductivity. Additionally, the 3.23 wt% PEG/WO_3-rG/SA membrane exhibited the highest initial conductivity among all tested membranes, reaching 2.33×10^{-1} S cm^{-1} at 25 °C. However, its conductivity decreased rapidly with increasing temperatures, dropping to 3.58×10^{-3} S cm^{-1} at 80 °C and 1.83×10^{-3} S cm^{-1} at 145 °C. The drastic drop indicates that while PEG enhances conductivity at lower temperatures by increasing membrane flexibility and water retention, its impact starts to appear less at elevated temperatures, possibly due to the decomposition of PEG.

Finally, the 2.74 wt% IL/PEG/WO_3-rG/SA membrane demonstrated moderate initial conductivity of 8.92×10^{-3} S cm^{-1} at 25 °C. At 80 °C, the conductivity slightly decreased to 3.84×10^{-3} S cm^{-1}, and remained relatively stable at 3.88×10^{-3} S cm^{-1} at 145 °C. In the PEG/WO_3-rG/SA membrane, the conductivity decreased at high temperatures due to dehydration and loss of hydrated pathways, and possibly due to the decomposition of PEG. The presence of [DEMA][OMs] IL contributes to hydrogen-bond networks, enhances water retention, and provides thermal stability, thus lowering the conductivity decrease effect. On the other hand, the observed decline in conductivity at higher temperatures correlates with reductions in WU. The dehydration process decreases the number of available proton carriers and interrupts the hydrogen-bonding networks. These combined effects explain why the conductivity of PEG/WO_3-rG/SA decreased at high temperatures. The IL/PEG/WO_3-rG/SA membrane exhibited the

most stable performance, due to the presence of the IL component, which decomposes at higher temperatures. The TGA, as seen in Fig. S-6, also showed the thermal stability of the IL-based membranes above the boiling point of water and up to 200 °C, especially for the ones that contain PEG and IL. However, its absolute conductivity at 145 °C remains below the 0.01–0.1 S cm^{-1} that is usually selected for practical HT-PEMs. For comparison, Nafion, the conventional membrane for PEMFCs, suffers from severe conductivity loss under anhydrous high-temperature conditions, often falling below 10^{-3} S cm^{-1} at ≥120 °C. In this context, the IL/PEG/WO_3-rG/SA membrane demonstrates improved conductivity retention relative to Nafion. However, additional optimization (*e.g.*, cross-linking or hybrid fillers) is still necessary to reach true HT-PEM performance. Accordingly, these conductivity trends can be explained by the coexistence of vehicle and Grotthuss transport mechanisms. At lower temperatures, proton motion is dominated by the vehicle process, where protons migrate together with water or ionic liquid species.[50] Upon increasing the temperature, enhanced segmental motion of polymer chains and stronger hydrogen-bonded networks would indeed favor the hopping of protons (*i.e.*, the Grotthuss mechanism),[51] which accounts for the more stable conductivity observed in IL/PEG/WO_3-rG/SA compared to PEG/WO_3-rG/SA.

3.5 Fourier transform infrared spectroscopy analysis

Fig. 7 displays the FTIR spectra of SA and its composite membranes. For the pristine SA sample (black line), a broad and intense peak centered around 3420 cm^{-1} corresponds to O–H stretching vibrations, which is characteristic of hydroxyl groups present in alginate chains.[16] This peak is consistently present in all composite membranes, indicating the retention of the hydroxyl functionality. Additionally, a weak band near 2923 cm^{-1} is attributed to the symmetric and asymmetric C–H stretching of methylene groups, which becomes slightly more pronounced in PEG-containing membranes due to the presence of aliphatic –CH_2– units.[46] The absorption peaks observed around 1591 cm^{-1} and 1417 cm^{-1} in all samples are also assigned to the asymmetric and symmetric stretching vibrations of the carboxylate –COO– groups in sodium alginate, respectively.[19] These bands exhibit minor shifts and intensity changes upon the incorporation of WO_3 and other additives. Specifically, in WO_3/SA (red line), a slight shift in the asymmetric –COO– stretching band toward lower wavenumbers was observed, which suggests potential coordination between WO_3 and carboxylate groups, indicating interaction between the metal oxide and the polymer matrix. In the IL/WO_3/SA spectrum (blue line), the broad O–H peak remains unchanged, but notable modifications appear in the –COO– stretching region. The asymmetric band slightly shifts to ~1585 cm^{-1}, while the symmetric one shifts to ~1410 cm^{-1}, suggesting stronger electrostatic interactions between the IL cations and the carboxylate groups.[10] Furthermore, a slight broadening in the region around 1200–1000 cm^{-1} is observed, corresponding to overlapping contributions from C–O stretching and S=O stretching, indicating possible incorporation of the IL anion

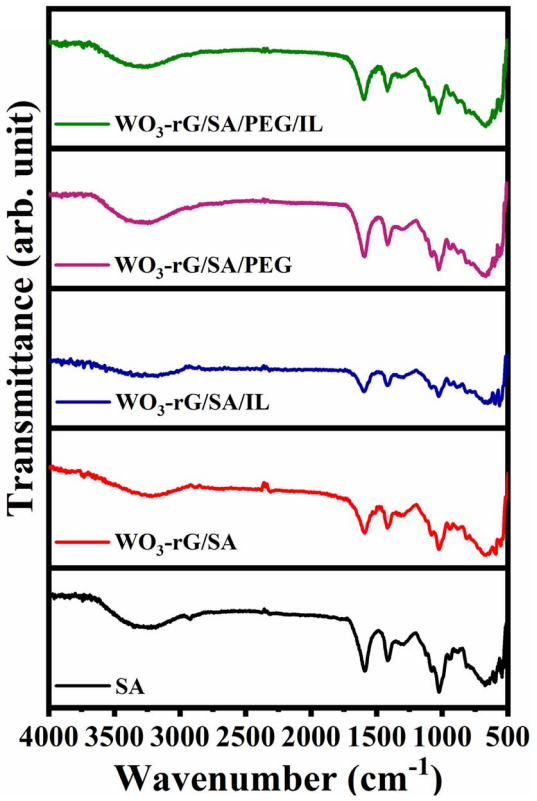

Fig. 7 FTIR spectra of SA membrane, WO_3-rG/SA membrane, IL/WO_3-rG/SA membrane, PEG/WO_3-rG/SA membrane, and IL/PEG/WO_3-rG/SA membrane (*x*-axis is the wavelength in cm^{-1} and *y*-axis is transmittance (a.u)).

functionalities. For the PEG/WO_3/SA membrane (pink line), the peak at 3420 cm^{-1} becomes broader compared to pristine SA, due to the presence of multiple hydroxyl groups in PEG and enhanced hydrogen bonding. A distinct peak at 1085 cm^{-1} appears, which is attributed to C–O–C stretching in PEG, confirming its incorporation. Similarly, the 2923 cm^{-1} peak intensifies, consistent with PEG's aliphatic chains. Finally, the IL/PEG/WO_3/SA membrane (green spectrum) shows combined features of both IL and PEG incorporation. A more intense and broader O–H peak at ~3420 cm^{-1} suggests extensive hydrogen bonding. Additional minor peaks appear in the 500–900 cm^{-1} region across all WO_3-containing spectra, especially around 670 and 811 cm^{-1}. These are attributed to the stretching vibrations of W–O and bending modes of W–––W, confirming the presence of tungsten oxide in the hybrid membranes.

3.6 Mechanical strength and performance

The mechanical properties of the fabricated membranes were assessed by measuring tensile strength, Young's modulus, and elongation at break, as shown in Table 4. Nafion 117 displays a tensile strength of 17.1 MPa, a Young's modulus of 205 MPa, and an elongation at break of 35%, reflecting a well-balanced combination of rigidity and flexibility. In comparison, the unmodified SA membrane displayed a tensile strength of 11.4 MPa and a high Young's modulus of 972.99 MPa, with a low

Table 4 Mechanical stability results of the membranes

Membrane	Thickness (μm)	Tensile strength (MPa)	Young modulus (MPa)	Elongation to break (%)	Ref.
Nafion 117	—	17.1	205	35	41
SPEEK	130	22.14	9.7	2.28	42
SA	200	11.4	972.99	2.30	This work
WO_3-rG/SA	200	3.21	679.3	0.95	This work
PEG/WO_3-rG/SA	200	6.244	1136.91	0.98	This work
IL/WO_3-rG/SA	200	6.55	1239.9	0.91	This work
IL/PEG/WO_3-rG/SA	200	2.95	1.047	768.1	This work

elongation of 2.30%, suggesting a rigid and relatively brittle structure. When incorporating WO_3-G into the SA matrix, both the tensile strength and elongation were reduced to 3.21 MPa and 0.95%, respectively, while the Young's modulus remained relatively high at 679.3 MPa, indicating increased brittleness and reduced elasticity. The introduction of PEG into the composite slightly enhanced tensile strength to 6.244 MPa and increased stiffness, as reflected by a Young's modulus of 1136.91 MPa, though the elongation remained low at 0.98%. On the other hand, the addition of IL to the WO_3-G/SA membrane further improved mechanical strength to 6.55 MPa and increased the Young's modulus to 1239.9 MPa. However, the elongation to break remained limited at 0.91%, indicating a stiffer but less flexible membrane. Notably, the IL/PEG/WO_3-rG/SA membrane showed an inverse behavior, with an extremely high elongation at break of 768.1% but much lower tensile strength and stiffness, measured at 2.95 MPa and 1.047 MPa, respectively. This dramatic increase in flexibility suggests that PEG and IL act synergistically to soften the membrane matrix and enhance its deformability. When compared to the typical relationship between mechanical properties and swelling behavior, these findings align well, as membranes with higher SR tend to show reduced tensile strength and stiffness but increased elongation, as observed with IL/PEG/WO_3-rG/SA. Conversely, membranes with low WU, such as the PEG/WO_3-rG/SA composition, exhibit greater rigidity and lower extensibility.[52]

4. Conclusions

This work reports the successful development and characterization of SA-based composite membranes reinforced with WO_3-rG that were further modified with PEG and IL ([DEMA][OMs]) for the application in HT-PEMFCs. The integration of WO_3-rG enhanced the conductivity significantly, as well as the thermal stability of the SA matrix. The presence of PEG further improved membrane flexibility and water retention, which appeared as a noticeable increase in room-temperature proton conductivity, with the PEG/WO_3-rG/SA membrane achieving a maximum value of 2.33×10^{-1} S cm^{-1} at 25 °C. Although the addition of IL alone reduced conductivity at higher concentrations, its interaction with PEG in the IL/PEG/WO_3-rG/SA membrane resulted in the most thermally stable conductivity pattern at elevated temperatures, maintaining 3.88×10^{-3} S cm^{-1} at 145 °C. This composition also demonstrated the highest ion exchange capacity of 1.65 meq g^{-1} and exceptional mechanical flexibility, indicating its suitability for a wide range thermal and mechanical stresses. The results highlight the potential of naturally derived, eco-friendly biopolymer matrices when functionally enhanced with nanostructured inorganic fillers and ion-conducting dopants. However, the high SR observed in IL/PEG/WO_3-rG/SA suggests a trade-off between the conductivity and the "dimensional" stability, indicating that further optimization is required. Future work should focus on evaluating controlled cross-linking strategies or hybrid nanofillers to mitigate excessive swelling while preserving high anhydrous conductivity. It should be noted that this study did not include durability assessments, such as long-term conductivity stability, thermal ageing, or chemical stability tests. These will be considered in future work to evaluate the membranes' suitability more fully for HT-PEMFC applications. Overall, this work provides a characterization study for the next-generation fuel cell systems.

Conflicts of interest

There are no conflicts to declare.

Data availability

The authors declare that the data supporting the findings of this study are available within the paper. Should any raw data files be needed in another format they are available from the corresponding author upon reasonable request.

Supplementary information is available. See DOI: **https://doi.org/10.1039/d5ra05401j**.

Acknowledgements

This work was financially supported by the University of Sharjah through the targeted research grant project number: 23020406306 and Petrofac Endowed Chairs Funds at the American University of Sharjah. The authors also acknowledge the support of the Advanced Materials Research Lab at the University of Sharjah for the characterization of the materials used.

References

1 S. Ong, A. Al-Othman and M. Tawalbeh, Emerging technologies in prognostics for fuel cells including direct hydrocarbon fuel cells, *Energy*, 2023, **277**, 127721, DOI: 10.1016/j.energy.2023.127721.

2 A. Ali, A. Al-Othman and M. Tawalbeh, Grand Challenges in Fuel cell Technology towards Resource Recovery, *J. Resour. Recovery*, 2023, **1**(1), 1004, DOI: 10.52547/jrr.2211.1004.

3 P. Sharma and O. P. Pandey, Proton exchange membrane fuel cells: fundamentals, advanced technologies, and practical applications, in *PEM Fuel Cells*, Elsevier, 2022, pp. 1–24, DOI: 10.1016/B978-0-12-823708-3.00006-7.

4 M. Tawalbeh, S. Alarab, A. Al-Othman and R. M. N. Javed, The Operating Parameters, Structural Composition, and Fuel Sustainability Aspects of PEM Fuel Cells: A Mini Review, *Fuels*, 2022, **3**(3), 449–474, DOI: 10.3390/fuels3030028.

5 C. Y. Wong, *et al.*, Additives in proton exchange membranes for low- and high-temperature fuel cell applications: A review, *Int. J. Hydrogen Energy*, 2019, **44**(12), 6116–6135, DOI: 10.1016/j.ijhydene.2019.01.084.

6 G. Xu, *et al.*, Enabling high-temperature application of Nafion membrane via imitating ionic clusters in proton conduction channels, *Int. J. Hydrogen Energy*, 2024, **56**, 330–337, DOI: 10.1016/j.ijhydene.2023.12.190.

7 Y. Bai, *et al.*, New anhydrous proton exchange membranes based on polypyrrolone (PPy) for high-temperature polymer electrolyte fuel cells, *J. Power Sources*, 2023, **563**, 232823, DOI: 10.1016/j.jpowsour.2023.232823.

8 J. O. Leader, Y. Yue, M. R. Walluk and T. A. Trabold, Voltage degradation of high-temperature PEM fuel cells operating at 200 °C under constant load and start-stop conditions, *Int. J. Hydrogen Energy*, 2022, **47**(43), 18820–18830, DOI: 10.1016/j.ijhydene.2022.04.067.

9 Y. Yin, *et al.*, Enhanced proton conductivity of Nafion composite membrane by incorporating phosphoric acid-loaded covalent organic framework, *J. Power Sources*, 2016, **332**, 265–273, DOI: 10.1016/j.jpowsour.2016.09.135.

10 W. Wu, *et al.*, Introduction of polymeric ionic liquids containing quaternary ammonium groups to construct high-temperature proton exchange membranes with high proton conductivity and stability, *J. Colloid Interface Sci.*, 2024, **675**, 689–699, DOI: 10.1016/j.jcis.2024.06.195.

11 W. Nimir, A. Al-Othman and M. Tawalbeh, Unveiling zirconium phytate-heteropolyacids-ionic liquids membranes for PEM fuel cells applications up to 150 °C, *Int. J. Hydrogen Energy*, 2025, **107**, 3–14, DOI: 10.1016/j.ijhydene.2024.06.120.

12 T. M. Ahmed, A. Al Othman, A. Shamayleh and M. Tawalbeh, Water management and conductivity studies in novel polymer zirconium-based membranes for PEM fuel cells, *Case Stud. Chem. Environ. Eng.*, 2025, **11**, 101081, DOI: 10.1016/j.cscee.2024.101081.

13 S. Song, H. He, S. Chai and H. Li, Advanced Nafion/nanofiller composite proton exchange membranes for fuel cell applications, *Polymer*, 2024, **307**, 127241, DOI: 10.1016/j.polymer.2024.127241.

14 M. R. Berber and I. H. Hafez, Boosting the proton conductivity, chemical stability, and fuel cell performance of nafion membrane at high operating temperatures and low humidity levels by incorporating phytic acid, *Int. J. Hydrogen Energy*, 2024, **57**, 1126–1138, DOI: 10.1016/j.ijhydene.2024.01.079.

15 Md. H. Hasan, M. H. Jihad and Md. A. B. H. Susan, Biopolymers for Fuel Cells, *Bio-Based Polymers: Farm to Industry*, 2024, vol. 3: Emerging Trends and Applications, ch. 7, pp. 121–142, DOI: 10.1021/bk-2024-1487.ch007.

16 N. Shaari, S. K. Kamarudin, S. Basri, L. K. Shyuan, M. S. Masdar and D. Nordin, Enhanced Proton Conductivity and Methanol Permeability Reduction via Sodium Alginate Electrolyte-Sulfonated Graphene Oxide Bio-membrane, *Nanoscale Res. Lett.*, 2018, **13**(1), 82, DOI: 10.1186/s11671-018-2493-6.

17 S. Abouricha, *et al.*, Biopolymers-Based Proton Exchange Membranes For Fuel Cell Applications: A Comprehensive Review, *ChemElectroChem*, 2024, **11**(9), DOI: 10.1002/celc.202300648.

18 L. Zhu, H. Yang, T. Xu, L. Wang, J. Lei and C. Si, Engineered Nanochannels in MXene Heterogeneous Proton Exchange Membranes Mediated by Cellulose Nanofiber/Sodium Alginate Dual Crosslinked Networks, *Adv. Funct. Mater.*, 2025, **35**(19), 2419334, DOI: 10.1002/adfm.202419334.

19 B. Munavalli, A. Torvi and M. Karidurаganavar, A facile route for the preparation of proton exchange membranes using sulfonated side chain graphite oxides and crosslinked sodium alginate for fuel cell, *Polymer*, 2018, **142**, 293–309, DOI: 10.1016/J.POLYMER.2018.03.044.

20 B. Smitha, S. Sridhar and A. A. Khan, Chitosan–sodium alginate polyion complexes as fuel cell membranes, *Eur. Polym. J.*, 2005, **41**(8), 1859–1866, DOI: 10.1016/j.eurpolymj.2005.02.018.

21 Y. Li, W. Zhou, D. Li and J. Xu, Multifunctional non-stoichiometric tungsten oxides: Synthesis, properties and application, *J. Power Sources*, 2025, **631**, 236222, DOI: 10.1016/j.jpowsour.2025.236222.

22 J. Yang, Y. Li, Y. Huang, J. Liang and P. K. Shen, Dynamic conducting effect of WO3/PFSA membranes on the performance of proton exchange membrane fuel cells, *J. Power Sources*, 2008, **177**(1), 56–60, DOI: 10.1016/J.JPOWSOUR.2007.11.022.

23 Z. G. Shao, H. Xu, M. Li and I. M. Hsing, Hybrid Nafion–inorganic oxides membrane doped with heteropolyacids for high temperature operation of proton exchange membrane fuel cell, *Solid State Ionics*, 2006, **177**(7–8), 779–785, DOI: 10.1016/J.SSI.2005.12.035.

24 A. Selim, G. P. Szijjártó, L. Románszki and A. Tompos, Development of WO3–Nafion Based Membranes for Enabling Higher Water Retention at Low Humidity and Enhancing PEMFC Performance at Intermediate Temperature Operation, *Polymers*, 2022, **14**(12), 2492, DOI: 10.3390/polym14122492.

25 D. He, K. Cheng, T. Peng, X. Sun, M. Pan and S. Mu, Bifunctional effect of reduced graphene oxides to support active metal nanoparticles for oxygen reduction reaction and stability, *J. Mater. Chem.*, 2012, **22**(39), 21298, DOI: 10.1039/c2jm34290a.

26 M. Samancı and A. Bayrakçeken Yurtcan, Chemically and thermally reduced graphene oxide supported Pt catalysts prepared by supercritical deposition, *Int. J. Hydrogen Energy*, 2022, **47**(45), 19669–19689, DOI: 10.1016/j.ijhydene.2022.04.124.

27 R. M. Nauman Javed, A. Al-Othman, M. Tawalbeh and A. G. Olabi, Recent developments in graphene and graphene oxide materials for polymer electrolyte membrane fuel cells applications, *Renewable Sustainable Energy Rev.*, 2022, **168**, 112836, DOI: 10.1016/j.rser.2022.112836.

28 D. He, Y. Jiang, H. Lv, M. Pan and S. Mu, Nitrogen-doped reduced graphene oxide supports for noble metal catalysts with greatly enhanced activity and stability, *Appl. Catal., B*, 2013, **132–133**, 379–388, DOI: 10.1016/j.apcatb.2012.12.005.

29 G.-C. Ri, J.-S. Kim and C.-J. Yu, Role of Water Molecules in Enhancing the Proton Conductivity on Reduced Graphene Oxide under High Humidity, *Phys. Rev. Appl.*, 2018, **10**(3), 034018, DOI: 10.1103/PhysRevApplied.10.034018.

30 A. K. Prasad, J.-Y. Park, S.-H. Kang and K.-S. Ahn, Electrochromic Performances of rGO-WO3 Thin Film and Its Application as an Integrated Device Powered with Quantum Dot-Sensitized Solar Cells, *Electron. Mater. Lett.*, 2024, **20**(6), 756–766, DOI: 10.1007/s13391-023-00464-x.

31 M. Tawalbeh, A. Al-Othman, A. Ka'ki, S. Mohamad and M. Faheem Hassan, Starch-chitosan-ionic liquids-based composite membranes for high temperature PEM fuel cells applications, *Int. J. Hydrogen Energy*, 2024, **67**, 852–862, DOI: 10.1016/j.ijhydene.2023.12.161.

32 A. Al-Othman, *et al.*, Novel composite membrane based on zirconium phosphate-ionic liquids for high temperature PEM fuel cells, *Int. J. Hydrogen Energy*, 2021, **46**(8), 6100–6109, DOI: 10.1016/j.ijhydene.2020.02.112.

33 A. Pokprasert and S. Chirachanchai, Polymer electrolyte membrane with heterocyclic terminated poly(ethylene glycol) brushes: An approach to decorate proton conductive species on membrane surface, *J. Membr. Sci.*, 2017, **524**, 550–556, DOI: 10.1016/j.memsci.2016.11.070.

34 Y. Yildiz and A. Manzak, The Effect of a Hydrophilic Polymer on the Morphology of Polymeric Membranes and the Retention of Metals, *Water, Air, Soil Pollut.*, 2024, **235**(8), 517, DOI: 10.1007/s11270-024-07324-w.

35 A. U. Anuar, N. N. Bonnia, N. M. Jamil and N. D. N. Affandi, Graphene oxide based regenerated carbon waste tyre (rCB): Synthesis by modified Hummers method and characterization, *Mater. Today Proc.*, 2023, DOI: 10.1016/j.matpr.2023.02.280.

36 J. Li, J. He, Y. Huang, D. Li and X. Chen, Improving surface and mechanical properties of alginate films by using ethanol as a co-solvent during external gelation, *Carbohydr. Polym.*, 2015, **123**, 208–216, DOI: 10.1016/J.CARBPOL.2015.01.040.

37 R. Al Shaikh, A. Al-Othman, M. Tawalbeh, A. Shamayleh and P. Nancarrow, Development of MXene incorporated PVDF based membranes for an enhanced performance in higher temperature PEM fuel cells, *Process Saf. Environ. Prot.*, 2024, **189**, 985–994, DOI: 10.1016/j.psep.2024.06.126.

38 M. Tawalbeh, W. Nimir, A. Al-Othman and A. Ka'ki, High proton conduction in zirconium silicate/lignin/ionic liquids based- membranes for high temperature PEM fuel cells, *Process Saf. Environ. Prot.*, 2024, **190**, 779–791, DOI: 10.1016/j.psep.2024.07.094.

39 S. Wang, *et al.*, Proton-conducting amino acid-modified chitosan nanofibers for nanocomposite proton exchange membranes, *Eur. Polym. J.*, 2019, **119**, 327–334, DOI: 10.1016/j.eurpolymj.2019.07.041.

40 M. Tawalbeh, W. Nimir, A. Al-Othman and A. Ka'ki, Facile nanocellulose-lignin composite membranes for polymer electrolyte membrane fuel cells applications operating above the boiling point of water, *Int. J. Hydrogen Energy*, 2025, **136**, 938–947, DOI: 10.1016/J.IJHYDENE.2025.04.314.

41 R. Sigwadi, T. Mokrani, P. Msomi and F. Nemavhola, The Effect of Sulfated Zirconia and Zirconium Phosphate Nanocomposite Membranes on Fuel-Cell Efficiency, *Polymers*, 2022, **14**(2), 263, DOI: 10.3390/polym14020263.

42 D. Vidhyeswari, A. Surendhar and S. Bhuvaneshwari, Enhanced performance of novel carbon nanotubes - sulfonated poly ether ether ketone (speek) composite proton exchange membrane in mfc application, *Chemosphere*, 2022, **293**, 133560, DOI: 10.1016/j.chemosphere.2022.133560.

43 M. Tawalbeh, M. F. Hassan, A. Al-Othman, A. Ka'ki, and F. Almomani, Alginate Modified Biomaterial Membranes for Fuel Cells Applications, in *2024 Advances in Science and Engineering Technology International Conferences (ASET)*, IEEE, 2024, pp. 01–04, DOI: 10.1109/ASET60340.2024.10708737.

44 H. Lin, F. Zhou, C.-P. Liu and V. Ozoliņš, Non-Grotthuss proton diffusion mechanism in tungsten oxide dihydrate from first-principles calculations, *J Mater Chem A Mater*, 2014, **2**(31), 12280–12288, DOI: 10.1039/c4ta02465f.

45 M. P. M. Hanif, A. J. Jalilah, M. F. H. Anisah and A. Tilagavathy, Chitosan/polyethylene oxide (PEO) filled carbonized wood fiber conductive composite film, *Mater. Sci. Forum*, 2020, **1010**, 638–644, DOI: 10.4028/www.scientific.net/MSF.1010.638.

46 M. Tawalbeh, A. A. Ali and A. Al-Othman, Flexible collagen-based membranes for PEM fuel cells applications: A characterization study, *Int. J. Hydrogen Energy*, 2025, **128**, 186–196, DOI: 10.1016/J.IJHYDENE.2025.04.235.

47 M. K. Sinha and M. K. Purkait, Increase in hydrophilicity of polysulfone membrane using polyethylene glycol methyl ether, *J. Membr. Sci.*, 2013, **437**, 7–16, DOI: 10.1016/j.memsci.2013.03.003.

48 M. F. Hassan, A. Al-Othman, M. Tawalbeh, A. Ka'ki and S. Mohamad, Novel chitosan-ionic liquid immobilized membranes for PEM fuel cells operating above the boiling point of water, *Int. J. Hydrogen Energy*, 2024, **53**, 592–601, DOI: 10.1016/J.IJHYDENE.2023.12.098.

49 S. Kalaiarasi, M. Kavitha, P. Karpagavinayagam, C. Vedhi and R. R. Muthuchudarkodi, Tungsten oxide decorated graphene oxide nanocomposite: Chemical synthesis, characterization and application in super capacitors, *Mater. Today Proc.*, 2022, **48**, 282–289, DOI: **10.1016/J.MATPR.2020.07.207**.

50 K. Hirata, K. Akasaka, O. Dopfer, S. Ishiuchi and M. Fujii, Transition from vehicle to Grotthuss proton transfer in a nanosized flask: cryogenic ion spectroscopy of protonated *p* -aminobenzoic acid solvated with D_2O, *Chem. Sci.*, 2024, **15**(8), 2725–2730, DOI: **10.1039/D3SC05455A**.

51 I. Popov, *et al.*, Search for a Grotthuss mechanism through the observation of proton transfer, *Commun. Chem.*, 2023, **6**(1), 77, DOI: **10.1038/s42004-023-00878-6**.

52 M. Tawalbeh, W. Nimir, A. Al-Othman and A. Ka'ki, High proton conduction in zirconium silicate/lignin/ionic liquids based- membranes for high temperature PEM fuel cells, *Process Saf. Environ. Prot.*, 2024, **190**, 779–791, DOI: **10.1016/j.psep.2024.07.094**.